Journal of Materials Chemistry A

ROYAL SOCIETY OF CHEMISTRY

PAPER

View Article Online
View Journal | View Issue

Cite this: J. Mater. Chem. A, 2025, 13, 40090

Operando XPS and NEXAFS to link the OER mechanism with the fast electro-oxidation of organic pollutants on a porous $NiMnO_3$–rGO anode

Keyvan Mirehbar,[ab] Santosh Kumar,[c] Ignasi Sirés,[d] Jaime S. Sánchez,[ae] Georg Held,[c] Jesús Palma[a] and Julio J. Lado *[a]

Electro-oxidation is one of the most promising and eco-friendly technologies for water decontamination. However, its industrial application is still limited by the high cost, poor faradaic efficiency, low durability, and potential toxicity of common high-power oxidation anodes. These challenges have been addressed by developing a novel composite comprising a mixed metal oxide ($NiMnO_3$) and reduced graphene oxide (rGO). The $NiMnO_3$–rGO anode allowed the fast and complete removal of phenol. Among different highly porous substrates, graphite felt (GF) led to the highest energy efficiency, since the GF/$NiMnO_3$–rGO anode yielded 100% phenol removal within only 30 min at a current density as low as 10 mA cm^{-2}, which was accompanied by 85% COD removal at 120 min. This anode demonstrated excellent stability, maintaining 100% phenol removal efficiency across five consecutive cycles while also showing low energy consumption (60–65 Wh (kg COD)$^{-1}$). Operando X-ray photoelectron spectroscopy (XPS) and near-edge X-ray absorption fine structure (NEXAFS) analysis provided mechanistic insights. It is demonstrated that rGO shifts the $^{\bullet}OH$ production pathway towards the lattice oxygen mechanism (LOM), in contrast to the adsorbate evolution mechanism (AEM) observed for $NiMnO_3$ alone. This mechanistic shift supports the enhanced stability and sustained electrocatalytic activity, contributing to the high performance of the GF/$NiMnO_3$–rGO composite anode in the context of a more sustainable technology for treating organic contaminants.

Received 2nd July 2025
Accepted 17th October 2025

DOI: 10.1039/d5ta05337d

rsc.li/materials-a

1. Introduction

The contamination of water bodies by organic pollutants, originating from different sources such as industrial, agricultural, and urban/domestic activities, as well as from the reduced dilution capacity of natural water streams, poses a serious threat to both the environment and human health.[1–3] These pollutants, which include pharmaceuticals and personal care products, pesticides, or microplastics are often resistant to conventional water treatment methods.[4] Such persistence underscores the need for advanced remediation strategies. Advanced oxidation processes (AOPs) have gained prominence in water treatment, with electrochemical AOPs (*i.e.*, EAOPs) particularly noted for their high efficiency and eco-friendliness.[5–7] EAOPs are effective due to their ability to generate reactive hydroxyl radicals ($^{\bullet}OH$) on site, which break down complex, recalcitrant contaminants into simpler, less harmful compounds.[8–10]

Electro-oxidation (EO) process is one of the most prominent EAOPs due to its simplicity and rapid pollutant degradation, in which the oxygen evolution reaction (OER) plays a key. This is an electrochemical process that produces $^{\bullet}OH$ as an intermediate, proceeding through diverse mechanisms that depend on the nature of the catalyst surface.[11,12] In the adsorbate evolution mechanism (AEM), $^{\bullet}OH$ is formed as intermediate during the stepwise water oxidation reaction to yield O_2. This mechanism involves the adsorption of water molecules onto the catalyst surface, where hydroxyl ion (OH^-) is electrochemically oxidized to form adsorbed hydroxyl radical (*OH). This radical is further oxidized to yield highly reactive oxygen species (*O$^{\bullet}$), which can then interact with water molecules to form *OOH as an intermediate and, finally, oxygen (O_2).[13] The AEM is advantageous for

[a]Electrochemical Processes Unit, IMDEA Energy Institute, Avda. Ramón de La Sagra 3, 28935, Móstoles, Madrid, Spain. E-mail: julio.lado@imdea.org
[b]Escuela de Doctorado UAM, Centro de Estudios de Posgrado, Universidad Autónoma de Madrid, C/Francisco Tomás y Valiente, nº 2. Ciudad Universitaria de Cantoblanco, Spain
[c]Diamond Light Source, Harwell Science and Innovation Campus, Didcot, Oxfordshire, OX11 0DE, UK
[d]Laboratori d'Electroquímica dels Materials i del Medi Ambient, Departament de Ciència de Materials i Química Física, Secció de Química Física, Facultat de Química, Universitat de Barcelona, Martí i Franquès 1-11, 08028 Barcelona, Spain
[e]Sungrow Power Supply Co., Ltd, No. 1699 Xiyou Rd, High-tech Industry Development Zone, Hefei, Anhui Province, China

pollutant degradation, as it continuously produces reactive species that directly contribute to organic pollutant cleavage. A different pathway is based on the so-called lattice oxygen mechanism (LOM), which involves the participation of lattice oxygen atoms within the catalyst material. Here, lattice oxygen (O_{latt}) atoms couple with adsorbed *OH or *O$^{\bullet}$ species, forming O–O bonds critical to OER. The LOM differs from AEM in the fact that it consumes lattice oxygen, which is subsequently replenished through electrochemical oxidation and deprotonation of OH^- ions.[13] This mechanism is highly dependent on the structural integrity and oxidation states of the catalyst, as lattice oxygen regeneration is essential for sustaining the OER activity. The electrocatalytic efficiency in both AEM and LOM mechanisms relies significantly on metal centers within the catalyst material. Transition metals such as Fe, Ni, and Mn are known for their ability to facilitate electron transfer and stabilize intermediate radical species.[14,15] Such oxidation flexibility of metals supports the stepwise electron transfer needed for OER, as exemplified in biological systems like those where a Mn_4CaO_5 cluster plays a crucial role in the stepwise oxidation of water, resulting in O–O bond formation.[16] In synthetic catalysts, Ni and Mn provide a similar redox versatility, cycling through oxidation states that stabilize intermediates like *O$^{\bullet}$ and *OOH, thereby enhancing the radical formation and eventually boosting the pollutant degradation efficiency.

In the EO process, the anode material is crucial, as it influences the efficiency of OER and the availability of reactive species. Conventional anode materials, such as PbO_2, boron-doped diamond (BDD), SnO_2, and other metal oxides are known as high-oxidation power anodes with great effectiveness,[17–22] but they face limitations due to their high cost, scarcity, and environmental concerns, especially toxicity.[23,24] Considering these constraints, there is a demand for new anode materials that not only maintain high pollutant degradation efficiency over prolonged use but also address economic and environmental challenges.

This study aims to meet these demands by proposing a novel anode design, consisting of a composite prepared with $NiMnO_3$, acting as an electrocatalytic mixed metal oxide (MMO), and reduced graphene oxide (rGO) to improve the electrical conductivity and accommodate the possible volume change.[25] Furthermore, the enhanced surface area provided by rGO is expected to increase the redox activity of $NiMnO_3$, thereby stabilizing the active intermediates over extended periods. The ultimate goal is to improve pollutant degradation efficiency and electrode durability. In previous research, we demonstrated that a nickel foam (NF) substrate coated with $NiMnO_3$ could achieve a high degree and rate of organic pollutant degradation; however, it exhibited limitations in long-term stability.[26] Additionally, in the present work, we have explored various substrates, including graphite felt (GF), aluminum foam (AF), and reticulated vitreous carbon (RVC), to optimize the structural composition further. Notably, few investigations have employed *in situ* or *operando* spectroscopic techniques to elucidate the mechanisms governing the EO process, particularly for the degradation of organic pollutants. Here, direct analysis using *operando* X-ray photoelectron spectroscopy (XPS) and near-edge X-ray absorption fine structure (NEXAFS) has been performed on $NiMnO_3$ and $NiMnO_3$–rGO coatings under reaction conditions, thereby revealing the dominant route of $^{\bullet}$OH production. This systematic strategy not only underscores the novelty of such real-time mechanistic insights but also demonstrates the strong performance and durability of the coating, key features for effective and long-lasting water treatment applications.

2. Experimental section

2.1. Synthesis of $NiMnO_3$–rGO composite

The $NiMnO_3$–rGO nanocomposites were produced using an efficient hydrothermal process coupled with subsequent thermal treatment, as shown in the sequence illustrated in Fig. 1. Initially, GO nanosheets were uniformly dispersed in 500 ml of Milli-Q water using an ultrasonic homogenizer (Hielscher, UP400S) for 20 min, resulting in a stable GO suspension. Following this, equal molar quantities of $Ni(NO_3)_2 \cdot 6H_2O$ and $Mn(NO_3)_2 \cdot 4H_2O$ were added and thoroughly mixed into this suspension, and then stirred continuously for 3 h, yielding a clear solution. Afterward, a 25 ml of 1.0 M sodium hydrogen carbonate ($NaHCO_3$) was swiftly mixed into the above mixture. The mixture was stirred for 2 h and, subsequently, transferred to a 500 ml Teflon-lined stainless-steel autoclave for the hydrothermal reaction, which was carried out at 150 °C for 12 h. After cooling to ambient temperature, the product was collected by centrifugation, washed several times with Milli-Q water and ethanol, and dried overnight at 80 °C. The dried precipitate was then calcined in a furnace at 450 °C (at a heating rate of 5 °C per minute) for 5 h to produce the $NiMnO_3$–rGO nanocomposite. Moreover, for comparison, pure $NiMnO_3$ and rGO samples were synthesized using the same procedure except GO was excluded in the pure oxide sample, and metal precursors were excluded in the rGO sample.

2.2. Surface characterization of powder nanocatalysts

To elucidate the crystallographic properties of the synthesized materials, we employed X-ray diffraction (XRD) analysis, conducted using a PANalytical Empyrean diffractometer. The equipment utilized Cu Kα radiation (wavelength = 1.54 Å) and was performed at a scan rate of 0.2° per second, with the radiation generated under conditions of 45 kV and 40 mA. For the examination of the morphological features and particle distribution in the samples, we utilized scanning electron microscopy (SEM) with a Hitachi TM-1000 microscope, and transmission electron microscopy (TEM) with a Philips Tecnai 20 microscope, the latter operating with a BaF_6 filament at an acceleration voltage of 200 kV. The Raman spectral analysis was executed at ambient temperature utilizing a JASCO NRS-5100 series Raman spectrometer, which excited the samples at a wavelength of 532 nm. To determine the carbon content in the samples, thermogravimetric analysis (TGA) was employed. This analysis involved heating the sample in an air atmosphere at a rate of 10 °C per minute, starting from room temperature and

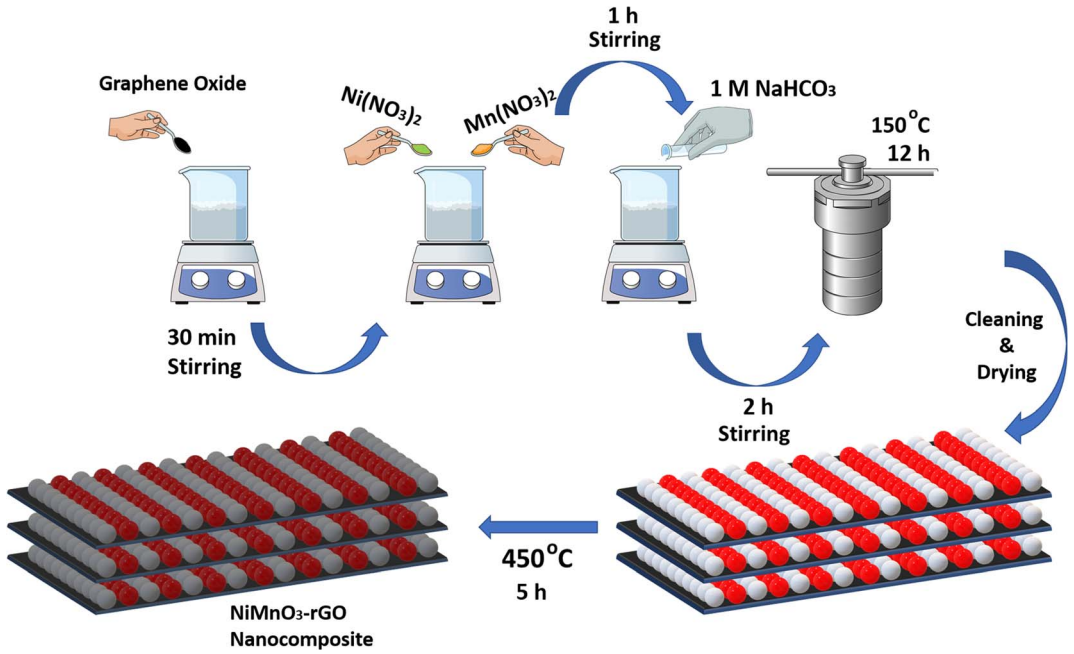

Fig. 1 Schematic illustration of the synthesis of the $NiMnO_3$–rGO nanocomposites.

reaching up to 700 °C, using an SDT Q-600 instrument from TA Instruments. Furthermore, the specific surface area and pore size distribution of the samples was measured. This measurement was based on the multipoint Brunauer–Emmett–Teller (BET) method and the Barrett–Joyner–Halenda (BJH) technique, respectively, applied to N_2 adsorption/desorption isotherms. These measurements were conducted using a Quantachrome QuadraSorb-S instrument.

Finally, the surface and near-surface composition of the $NiMnO_3$–rGO samples was investigated through *ex situ* and *in situ operando* XPS and NEXAFS spectroscopy. These experiments were performed at the Versatile Soft X-ray (VerSoX) beamline B07 at the Diamond Light Source, the UK's synchrotron radiation facility in Harwell Campus in Oxfordshire, UK. Near ambient pressure (NAP)-XPS and NEXAFS spectroscopy measurements were carried out in the Teacup Endstation of Branch C at the B07 beamline. A Nafion/C/Catalyst as a working electrode was mounted on the electrochemical flow cell for *operando* measurements, and NEXAFS spectra were recorded in total electron yield (TEY) mode at room temperature under high vacuum or 2 mbar water vapor using the 600 L mm^{-1} monochromator grating and an exit slit y-gap of 0.05. The photon energies were calibrated and normalized using I_0 characteristics (mesh current at Branch C). Furthermore, background correction was performed at lower photon energies and normalized to 1 at higher photon energies. On the other hand, for *operando* NAP-XPS measurements, a fixed photon energy of 1200 eV was used, using the 600 L mm^{-1} monochromator grating and an exit slit y-gap of 0.05 mm. This resulted in a beamline resolution (the broadening introduced by the monochromator) below 0.5 eV. A pass energy of 20 eV was used for high-resolution scans. The Fermi edge was used to calibrate the binding energies. The background was normalized to 1 for all spectra.

2.3. Electrochemical characterization

All electrochemical tests (cyclic voltammetry (CV), linear sweep voltammetry (LSV), and electrochemical impedance spectroscopy (EIS)) were conducted in a flow cell identical to that employed for the final application, thus closely replicating operating conditions and minimizing false positives. Nafion 117 was used as the separator in the cell. The setup was arranged in a two-electrode configuration, with the GF/$NiMnO_3$-based electrode serving as the working electrode and stainless steel acting as both counter and reference. A 0.1 M Na_2SO_4 solution at neutral pH served as the electrolyte. The electrochemical measurements were performed on a Bio-Logic VMP3 controlled by EC-Lab software. For CV and LSV analysis, the potential was swept from 0.25 V to 2.0 V (*vs.* stainless steel) at a scan rate of 10 mV s^{-1}. Electrochemical impedance spectroscopy was carried out over a frequency range of 100 k Hz to 100 m Hz, using a 5 mV amplitude.

2.4. Preparation of 3D composite anodes

Our study investigated various substrates to be coated with the nanocomposites, including RVC with differing pore sizes (10, 20, and 30 pores per inch (ppi)), AF (30 ppi), and GF. Substrate samples were cut to 20 mm × 20 mm × 6 mm and cleaned thoroughly by sonication in 0.1 M HCl solution, acetone, ethanol, and water for 10 min each. The ink for substrate coating was formulated by mixing 85 wt% active material, 10 wt% carbon black as a conductive agent, and 5 wt% polyvinylidene fluoride (PVDF) as a binder in *N*-methyl-2-pyrrolidone (NMP). As illustrated in Fig. S1, the substrates were immersed in the colloidal ink, sonicated for 30 min, and then pulled out and dried at 80 °C for 12 h. The mass loading of deposited particles on the different substrates was consistently determined as around 200 ± 5 mg.

2.5. Electro-oxidation process

As detailed in an earlier publication, a unique 3D-printed electrochemical cell has been designed for efficient pollutant removal.[26] This cell, fabricated from UV-sensitive resin (ANYCUBIC), featured a flow-through configuration where the electrolyte flow was perpendicular to the electric current flow between the anode and cathode. Central to the design is the 3D electrode, aimed at uniform current and potential distribution, minimal ohmic resistance, and optimized mass transport of electroactive species.

The cell comprised an expanded graphite plate (Sigracell TF6) as the current collector for the anode, positioned in the anolyte channel, and a thin stainless-steel plate (0.2 mm thickness, Goodfellow) in the cathodic compartment. A Masterflex® L/S peristaltic pump maintained a constant liquid flow rate, with a 4 mm interelectrode gap and a Nafion 117 membrane (Ion Power) separating the anolyte and catholyte. This design, as reported in our earlier study, significantly advances electrochemical cell technology for water treatment applications.[26]

To study the electrochemical oxidation of phenol, experiments were conducted using a 0.1 M Na_2SO_4 (Sigma-Aldrich) solution as the supporting electrolyte. A variety of electrodes, namely NF/$NiMnO_3$, NF/$NiMnO_3$–rGO, GF/$NiMnO_3$, GF/$NiMnO_3$–rGO, AF/$NiMnO_3$, and RVC/$NiMnO_3$ were employed as anodes. Each of them was consistently paired with a stainless-steel sheet serving as the cathode. The other experimental parameters included an initial phenol (Sigma-Aldrich) concentration of 100 mg L^{-1}, equal anolyte and catholyte volumes of 100 mL, a flow rate maintained at 30 mL min^{-1}, and a solution pH of approximately 6.0 (*i.e.*, natural pH of the treated solution).

The chemical oxygen demand (COD) of the solutions under study was determined by employing commercial kits from Merck (ISO 15705) on a Spectroquant® Prove 100 VIS spectrophotometer. In turn, the phenol concentration was measured by UV/Vis spectroscopy on a PerkinElmer (model LAMBDA 1050 WB InGaAs) spectrophotometer that was set at λ between 190 to 350 nm.

3. Results and discussion

3.1. Structural and morphological investigation

The structural characterization and phase identification in the samples obtained after heat treatment (5 h at 450 °C) were systematically carried out *via* powder XRD measurements, as shown in Fig. 2a. The diffraction peaks detected in the $NiMnO_3$ sample were consistent with those of the rhombohedral ilmenite phase, which corresponds to JCPDS Card No. 98-001-3753 and is categorized as $R\bar{3}$.[27] Notably, similar peaks were also clearly visible in the $NiMnO_3$–rGO nanocomposite sample. The prominent first peak in $NiMnO_3$–rGO results from overlap with rGO characteristic diffraction at a similar 2θ position, making the (110) reflection appear more intense than in pure $NiMnO_3$. rGO typically exhibits a broad reflection around 24–26°, depending on reduction conditions and stacking order. These findings confirm that the crystalline structure remained essentially unchanged during the hybridization process. Further insights into the structural nuances were gained through Raman spectroscopy, as illustrated in Fig. 2b. The spectra for both $NiMnO_3$ and the $NiMnO_3$–rGO nanocomposite exhibited characteristic peaks within the 200–700 cm^{-1} range, attributable to metal–oxygen bonding vibrations. Notably, the $NiMnO_3$–rGO nanocomposite spectrum exhibited additional bands at 1329 cm^{-1} and 1583 cm^{-1}, corresponding to the D and G bands of carbonaceous structures, respectively. The D band is associated with structural defects in sp^2-hybridized carbon domains, whereas the G band is attributed to the first-order scattering of the E_{2g} vibrational mode in graphitic carbon.[28] A noteworthy observation is the lower I_D/I_G ratio in the nanocomposite (0.90) as compared to that of pure rGO (0.98), suggesting a successful reduction of GO to rGO. The distinct peaks at 542 and 611 cm^{-1} are attributed to the MnO vibrational modes, and those at approximately 370 and 1050 cm^{-1} likely correspond to Ni–O bonding.[29] TGA curves provided quantitative insights into the composition of the nanocomposites (Fig. 2c). The curve for pure $NiMnO_3$ exhibited a marginal mass loss of approximately 1%, likely due to the release of lattice-incorporated water or surface-adsorbed hydroxyl groups. Conversely, the pure rGO sample demonstrated a near-complete mass loss upon heating to 500 °C, confirming its decomposition. For the $NiMnO_3$–rGO nanocomposite, an abrupt mass loss was observed between 500 °C and 600 °C, attributable to the combustion and decomposition of the rGO component, allowing for an estimation of the $NiMnO_3$ mass content at around 80% in the nanocomposite.

The high-resolution XPS spectra of Ni 2p, Mn 2p, C 1s, and O 1s of $NiMnO_3$–rGO sample, obtained from the survey scan (Fig. S3), are shown in Fig. 2d–f. Ni 2p scan (Fig. 2d) indicates that nickel exists in its mixed state Ni^{2+} (854.7 eV and 857.9 eV)/Ni^{3+} (855.9 eV) at the surface of $NiMnO_3$–rGO sample. In addition, the shakeup satellite peak was also observed at 7 eV above the main emission line for Ni $2p_{3/2}$ due to the presence of Ni^{2+}. The Mn 2p scan (Fig. 2e) confirms the presence of Mn^{3+} (639.5 eV) and Mn^{4+} (642.0 eV). Similarly, the binding energy peaks in the O 1s scan were positioned at 529.9, 531.3, and 533.2 eV corresponding to metal–O–metal (M–O–M), hydroxides (OH^-), and adsorbed water molecules (H_2O), respectively (Fig. 2f). Thus, the resultant phases are the oxyhydroxides of Ni and Mn. The apparent higher quality of the O 1s spectra arises primarily from the stronger signal of surface-adsorbed oxygen species, compared to the relatively weaker lattice oxygen contribution. In contrast, the Ni 2p and Mn 2p spectra inherently display lower signal-to-noise ratios, which can be attributed to the lower photoemission cross-sections of Ni and Mn and the presence of complex multiplet splitting. These factors make the transition-metal spectra appear noisier, even though they were acquired under identical measurement conditions. The C 1s spectra of rGO ($NiMnO_3$–rGO) exhibits three major components at 288.8, 286.1, 284.6 eV, which can be indexed to the O=C–O, C–O, and C–C, respectively (Fig. S4). The XPS results provide evidence of the surface oxidation states of the metallic centers in the synthesized $NiMnO_3$–rGO and the existing bonds on the surface

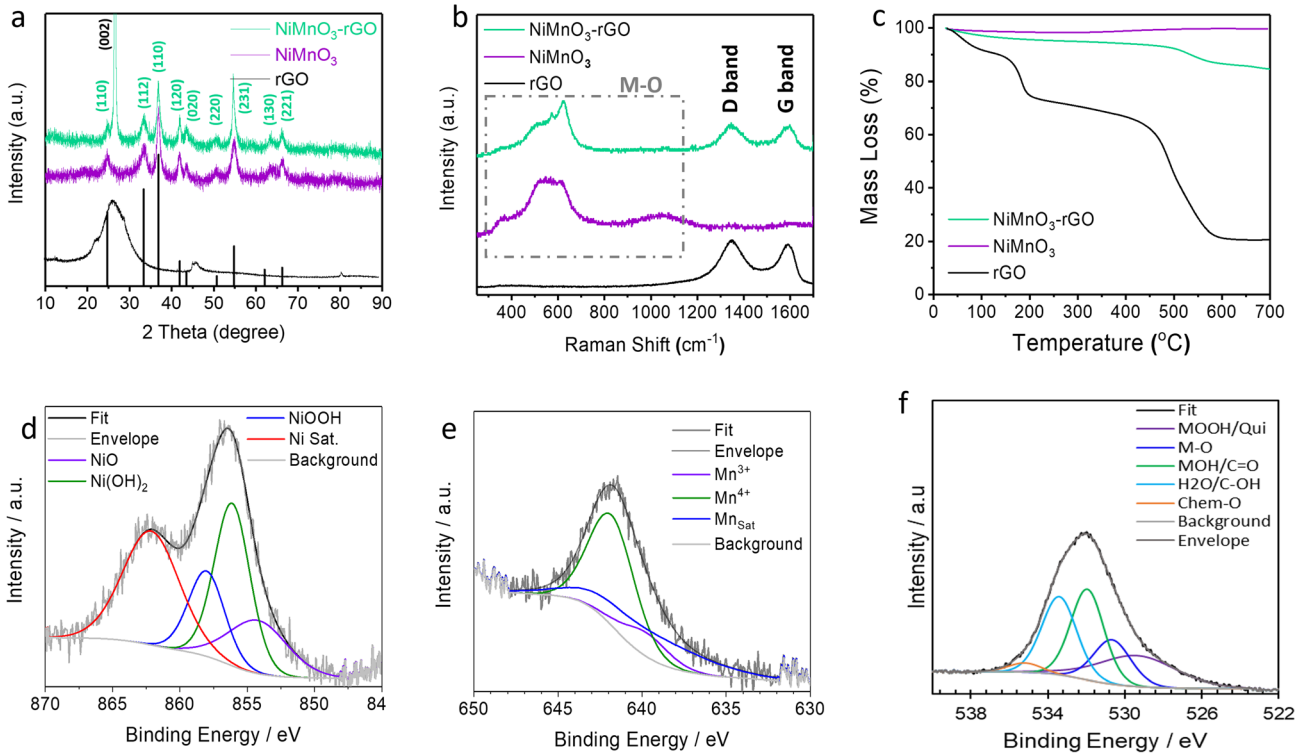

Fig. 2 Structural and physicochemical characterization of the $NiMnO_3$–rGO, $NiMnO_3$, and rGO samples: (a) microstructural XRD analysis. (b) Raman spectroscopy. (c) TGA curves. (d–f) *Ex situ* XPS spectra of (d) Ni 2p, (e) Mn 2p, (f) O 1s for $NiMnO_3$–rGO.

of this material. Note that Fig. 2f shows the clear overlapping contributions such as O=C/M–O and C–O/M–H_2O.

SEM imaging of the $NiMnO_3$–rGO nanocomposite is presented in Fig. 3a, offering a detailed morphological perspective. The micrographs reveal that the composite predominantly comprises particles of a few micrometers, exhibiting irregular shapes. This morphological characteristic is likely a result of the attachment of small metal oxide nanoparticles onto larger rGO flakes, approximately 20 nm in size. Notably, a certain degree of particle agglomeration was observed, which is hypothesized to have occurred during the drying phase of the sample preparation. EDS analysis further complemented the SEM observations, confirming an equitable distribution of nickel (Ni), manganese (Mn), and oxygen (O) elements across the surface of the nanocomposite. Additionally, a carbon (C) content of approximately 15% was identified through EDS, corroborating the findings obtained from TGA curves. This good agreement between EDS and TGA results underscores the reliability of our compositional analysis and provides a comprehensive understanding of the elemental distribution in the nanocomposite.

TEM analyses were conducted to elucidate the distribution of oxide nanoparticles on the rGO nanosheets within the $NiMnO_3$–rGO nanocomposite. Fig. 3b reveals the rGO nanosheets, characterized by their thin-layered structure with noticeable surface wrinkling. However, identifying distinct crystalline domains on these nanosheets proved challenging. Enhanced magnification, as displayed in Fig. 3c, provides a clearer view of the carbon network surface. It is densely and uniformly covered with $NiMnO_3$ nanoparticles, each approximately 2.5 nm in diameter (Fig. 3d). This uniformity suggests a robust anchoring of nanoparticles across the surface of the conductive rGO layers. The nanoparticles appear to lack defined boundaries, and their agglomeration contributes to the nanoporous architecture of the nanocomposite. An intriguing observation from Fig. 3e is the uneven decoration of the rGO edges with $NiMnO_3$ nanoparticles, potentially due to a preferential attachment of metal oxides to the basal plane of rGO, which is rich in epoxide and hydroxyl groups, as opposed to the edges featuring carboxyl and carbonyl groups. This distribution and the potential interaction of the nanoparticles with the rGO matrix is expected to become crucial to boost the electrochemical performance of the material.[30] The intimate association between the nanoparticles and rGO enhances conductivity and shortens ion transport pathways.[31] Such a configuration facilitates redox reactions, significantly impacting the overall electrochemical response.[32] This microscopic insight into the nanocomposite structure provides a valuable understanding of its functional properties and potential applications in electrochemical systems.

3.2. Electrochemical performance

The electrochemical performance of pure GF/$NiMnO_3$ and GF/$NiMnO_3$–rGO composite materials was evaluated using various electrochemical characterization techniques, including CV, LSV, Tafel slope analysis, and EIS. All measurements were conducted in an electrochemical flow cell designed for the

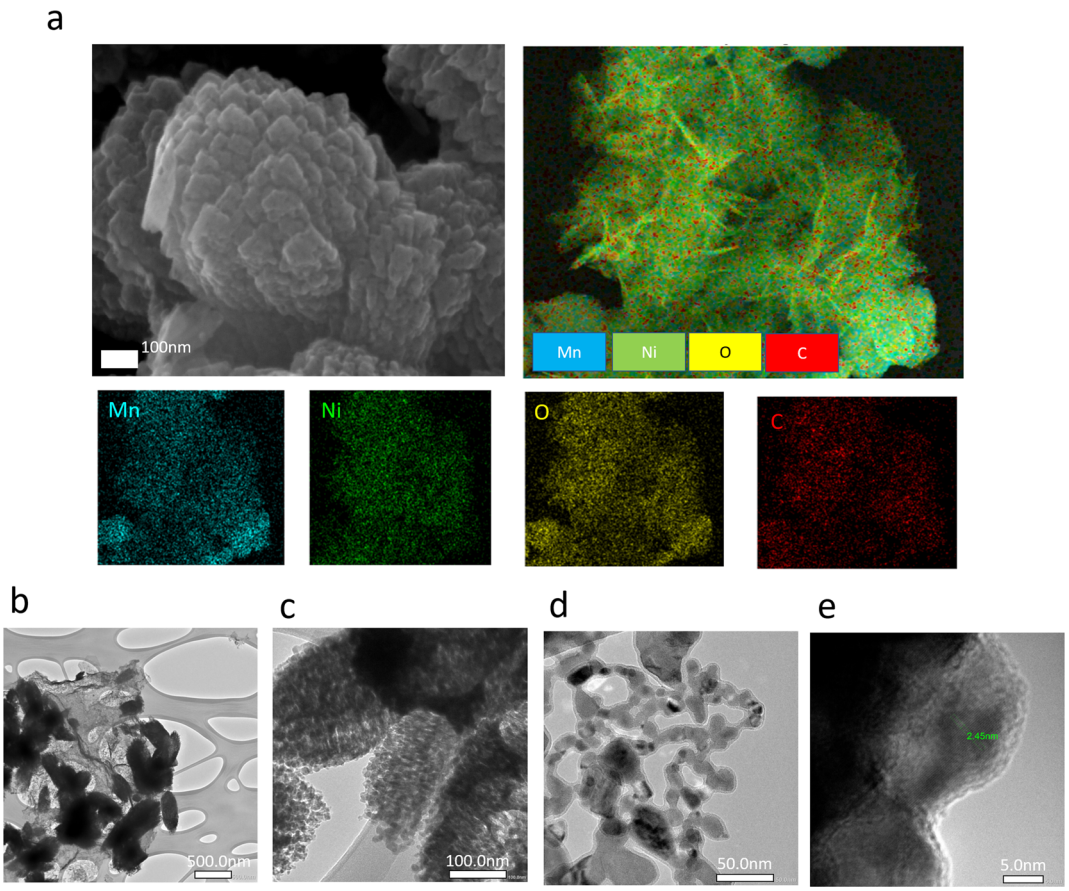

Fig. 3 Microscopical analysis of $NiMnO_3$–rGO. SEM images of (a) $NiMnO_3$–rGO plus mapping of the different elements (Ni, Mn, O, and C). (b–e) TEM images of $NiMnO_3$–rGO nanocomposite at different magnifications.

primary experiments. The CV analysis reveals an enhancement in the electrochemical activity of the $NiMnO_3$–rGO composite as compared to the pure $NiMnO_3$. As depicted in Fig. 4a, the $NiMnO_3$–rGO composite exhibits a higher current response across the potential range. This superior performance likely results from multiple synergistic effects associated with the incorporation of rGO, including enhanced electrical conductivity and an increased accessible surface area. BET measurements and pore size distribution (PSD) analysis revealed a higher proportion of small mesopores (2–5 nm) compared to the pure oxide, which likely facilitates ion transport through low-resistance pathways and provides shorter diffusion routes within the porous network.[31] This superior performance can be attributed to enhanced electrochemical activity, which stems from the increased conductivity and larger electrochemical surface area provided by the reduced graphene oxide (rGO) within the composite structure. The LSV results, shown in Fig. 4b, corroborate the findings from the CV analysis, demonstrating superior OER activity for the $NiMnO_3$–rGO composite. This material exhibits higher current densities at equivalent overpotentials compared to pristine $NiMnO_3$. Quantitative analysis revealed a lower Tafel slope for the composite (41 mV dec^{-1}) as compared to the pure electrocatalyst (49 mV dec^{-1}), indicating more efficient catalytic processes and faster electron transfer kinetics (Fig. 4c). Additionally, the Nyquist plots obtained from EIS measurements (Fig. 4d) show that the $NiMnO_3$–rGO composite exhibits a significantly smaller charge transfer resistance (R_{ct}) compared to the $NiMnO_3$. The impedance data were fitted to a three-element equivalent circuit model comprising the electrolyte resistance (R_e), a parallel combination of resistance (R_{ct}) and capacitance (C_{dl}), representing the charge transfer resistance and the double-layer capacitance, respectively. The reduced R_{ct} for the composite indicates a more efficient charge transfer at the electrode–electrolyte interface, facilitated by the conductive network formed by the rGO. The enhanced electrochemical behavior of the $NiMnO_3$–rGO composite can be attributed to its improved electrical conductivity as well as additional contributing factors, such as an optimized pore size distribution.[31] These features collectively support the initial hypothesis that modifying $NiMnO_3$ with rGO would enhance its electrochemical performance. The rGO within the composite provides a highly conductive network that facilitates faster electron transport, leading to higher current responses observed in CV, LSV, and smaller R_{ct} in the EIS analyses. Furthermore, the rGO sheets offer a high surface area that supports the $NiMnO_3$ particles, minimizing their agglomeration and offering more active sites for the OER. The increased current densities and lower Tafel slope indicate enhanced electrocatalytic efficiency.

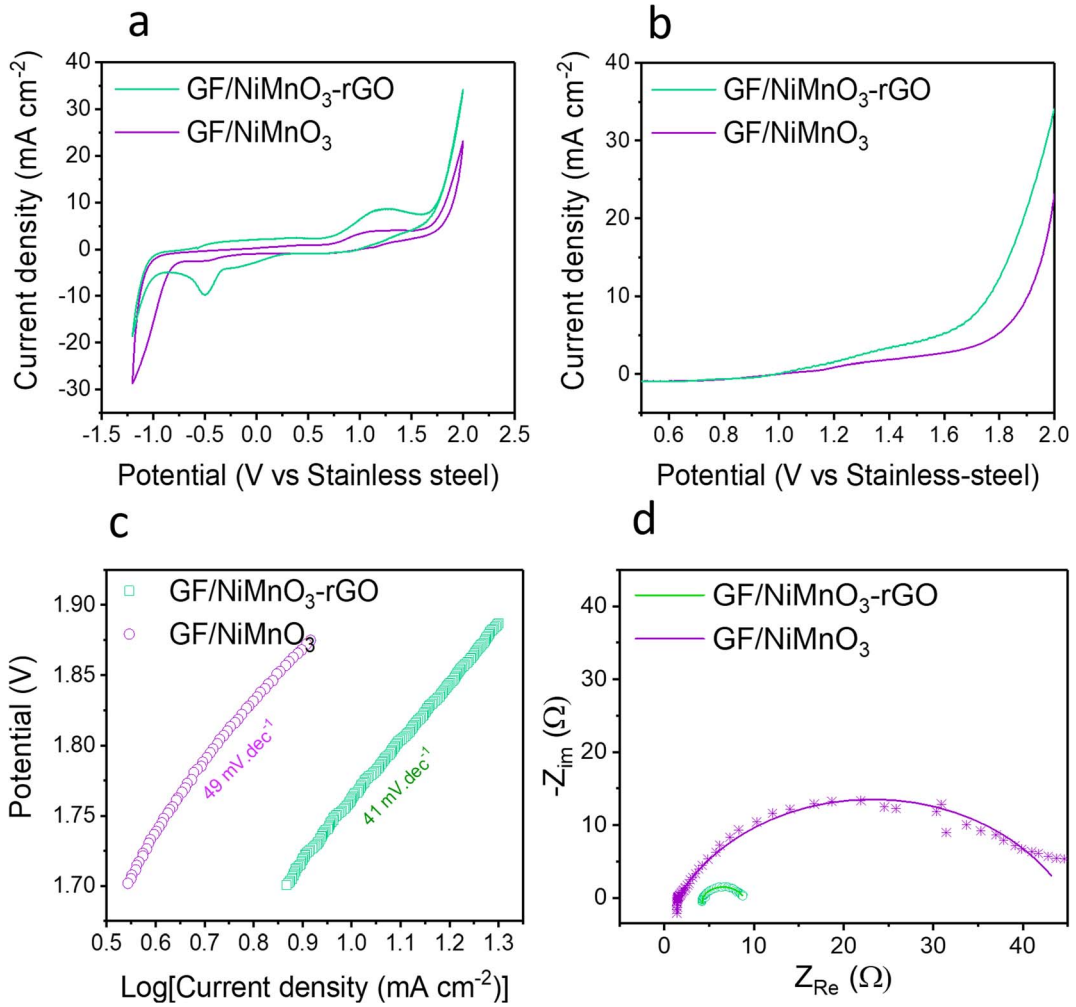

Fig. 4 Electrochemical characterization of $NiMnO_3$ and $NiMnO_3$–rGO performed in the electrochemical flow cell at a scan rate of 10 mV s^{-1} and 0.1 M Na_2SO_4 electrolyte solution at neutral pH. (a) CV, (b) LSV, (c) corresponding Tafel slopes, and (d) EIS.

3.3. Electrochemical oxidation of organic pollutants

In a series of experiments conducted within the electrochemical flow cell setup, a comparative analysis was undertaken to evaluate the performance of $NiMnO_3$–rGO composite against $NiMnO_3$. Initially, the performance of different substrates was analyzed using $NiMnO_3$ as active material (Section S4). Subsequently, both active materials, $NiMnO_3$ and $NiMnO_3$–rGO were systematically deposited on selected porous substrates (NF and GF) to assess their efficacy for phenol and COD removal (Fig. 5a–d). The results reveal that $NiMnO_3$–rGO electrodes significantly outperformed the $NiMnO_3$ electrodes across both substrates, validating our initial hypothesis that the incorporation of rGO would enhance the electrical conductivity and facilitate electron transfer, resulting in accelerated degradation rates. Although the final phenol conversion after 120 min is quite similar for both materials regardless of the supporting substrate (NF or GF), Fig. 5c clearly shows that the degradation of the target pollutant proceeds much more rapidly in the presence of rGO—approximately 90% of the pollutant is removed within the first 10 min, compared to only about 50% using the oxide alone—highlighting the decisive role of rGO in accelerating the reaction kinetics. Further *operando* XPS and NEXAFS measurements described in the following section were conducted to gain deeper insights into the mechanistic differences and the reasons behind the superior performance of $NiMnO_3$–rGO.

The comparative analysis of substrates highlights the superior performance of the GF/$NiMnO_3$–rGO electrodes, achieving nearly complete phenol removal (~100%) within 30 min, whereas NF/$NiMnO_3$–rGO electrodes required up to 60 min to reach similar efficiency (Fig. 5a and c). This result suggests a synergistic effect when using GF as a substrate in combination with rGO. Additionally, COD removal trends mirror these findings (Fig. 5b and d), indicating that GF/$NiMnO_3$–rGO is the most efficient in pollutant degradation.

In terms of energy consumption, all electrodes demonstrated low energy requirements, falling within the range of 60–65 Wh per kg of COD removed (Fig. 5e). In particular, the rGO-containing electrodes exhibited the lowest energy consumption values, underscoring the positive impact of rGO in reducing resistance and enhancing electron mobility, which translates

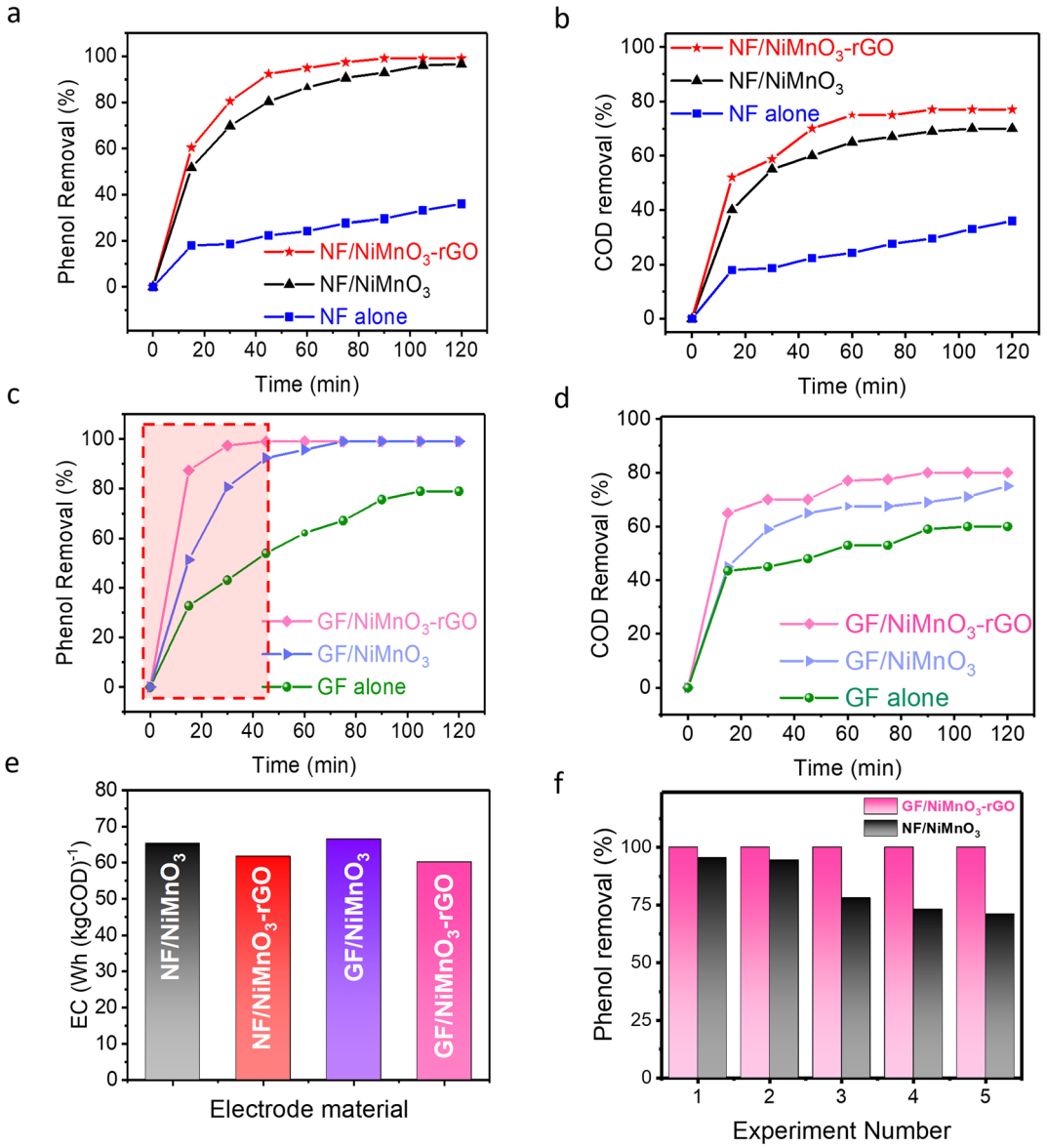

Fig. 5 (a) Comparison of phenol degradation using anodes with different active materials on nickel foam (NF) substrate, and (b) corresponding COD removal. (c) Comparison of phenol degradation using anodes with different active materials on graphite felt (GF) substrate and (d) corresponding COD removal. (e) Energy consumption (EC) using different anodes. (f) Reusability tests, showing the evolution of phenol removal in consecutive runs.

into lower operation costs. One of the most striking outcomes of this study was the exceptional stability demonstrated by the GF/$NiMnO_3$–rGO electrode. Stability assessments revealed an astonishing level of robustness, with the electrode maintaining its phenol removal efficiency virtually unchanged over five consecutive cycles of 2 h (Fig. 5f). This outstanding performance contrasts with the NF/$NiMnO_3$ electrodes, which suffered a significant efficiency decline of over 25% under identical conditions. These results highlight the superior stability advantages imparted by the GF substrate and rGO modification, establishing the GF/$NiMnO_3$–rGO electrode as a highly reliable and durable solution for phenol removal applications.

Based on these results, the GF/$NiMnO_3$–rGO electrode stands out as the most promising candidate, offering high removal efficiency, low energy consumption, and superior durability, making it an ideal choice for advanced EOPs targeting organic pollutants.

All experiments were conducted in 0.1 M Na_2SO_4 electrolyte (neutral pH) with an initial phenol concentration of 100 mg L^{-1}, operated at a current density of 10 mA cm^{-2}.

3.4. Structure–activity relationship

To further investigate the mechanistic variations and underlying factors contributing to the enhanced performance of $NiMnO_3$–rGO, additional *operando* XPS and NEXAFS analyses were performed. For *operando* investigations, the flow cell with the polymer-based working electrode assembly is mounted in

the "Tea-Cup" Endstation of the NAP-XPS/NEXAFS B07 beamline (Branch C) at Diamond Light Source synchrotron radiation. As shown in Fig. S6, the beam, analyzer cone, and sample surface meet in one flange and the angle between the incoming beam and the sample surface and the analyzer cone is 60° on the NAP-XPS/NEXAFS beamline.[33] To minimize the gas phase contribution, we moved the sample and analyzer cone along with the corresponding incoming beams using a sledge. The Nafion 115/C/Catalyst working electrode was investigated as a function of applied potential under OER conditions. In the case of $NiMnO_3$, the Ni 2p spectrum shows a switching between Ni^{2+} (NiO) and Ni^{2+} ($Ni(OH)_2$) species (Fig. 6a).[34] As can be observed in Fig. 6b, the peaks at 642.1 eV and 645.0 eV correspond to Mn^{3+} and Mn^{4+}, respectively. More intriguingly, when the anodic potential increased from OCP to OER, a new peak appeared at higher binding energy with decreasing intensity of peak at lower binding energy, indicating the oxidation of Mn^{3+} to Mn^{4+}. The O 1s spectrum of $NiMnO_3$ under OCP condition, shows in Fig. 6c a broad feature with three maxima at 534–530 eV, attributed to lattice oxygen (530.0 eV), adsorbed OH species (531.9 eV) and H_2O (533.2 eV). A strong and sharp peak at 535.3 eV is attributed to gas phase water molecules within the excitation volume between the sample and analyzer (*i.e.*, water vapor caused by external water dosing). The lattice oxygen peak evolves towards higher binding energy when anodic potential increases, indicating the formation of the M–O–H bond on the surface, which agrees with the shift observed in the Mn 2p spectra. An evolving feature above 533.0 eV in the O 1s spectra can also be identified at OER conditions (Fig. 6c), which could be due to the presence of M–O–O–H. The $NiMnO_3$ binds oxygen very strongly, resulting in the O–O bond formation step to generate the *OOH intermediate, being a rate-determining step for OER. In $NiMnO_3$–rGO sample, the Ni 2p spectrum shows a switching between Ni^{2+} (NiO) and Ni^{2+} ($Ni(OH)_2$) species (Fig. 6d), similar to the $NiMnO_3$ sample. It is very interesting that over $NiMnO_3$–rGO, when the anodic potential is increased from OCP to OER, surface Mn^{3+} is oxidized to Mn^{5+} (Fig. 6e) with reversible changes but no M–O–O–H formation (Fig. 6f), which is indicating the prevalence of LOM.[35]

Based on our *operando* XPS and NEXAFS analysis, the prevailing OER pathway on the pure $NiMnO_3$ electrocatalyst is consistent with the adsorbate evolution mechanism (AEM, Fig. 7a). This interpretation is supported by the observed redox transitions of Ni^{2+}/Ni^{3+} and Mn^{3+}/Mn^{4+} in Fig. 6, which indicate that oxygen evolution proceeds *via* surface-adsorbed intermediates. The AEM involves four concerted proton–electron transfer steps centered on the metal ions: initial OH^- adsorption at a surface vacancy, deprotonation to form O*, O–O bond formation *via* reaction with a second OH^-, and eventual release of O_2 while regenerating the active site.[36,37] In contrast, for GF/$NiMnO_3$–rGO, the *operando* spectra reveal a higher degree of lattice oxygen participation, as evidenced by the reversible changes in the O 1s and Mn L-edge features (Fig. 6d–f). These observations are consistent with the lattice oxygen mechanism (LOM, Fig. 7b), where O–O bond formation proceeds *via* coupling between lattice oxygen atoms. The free energy diagram

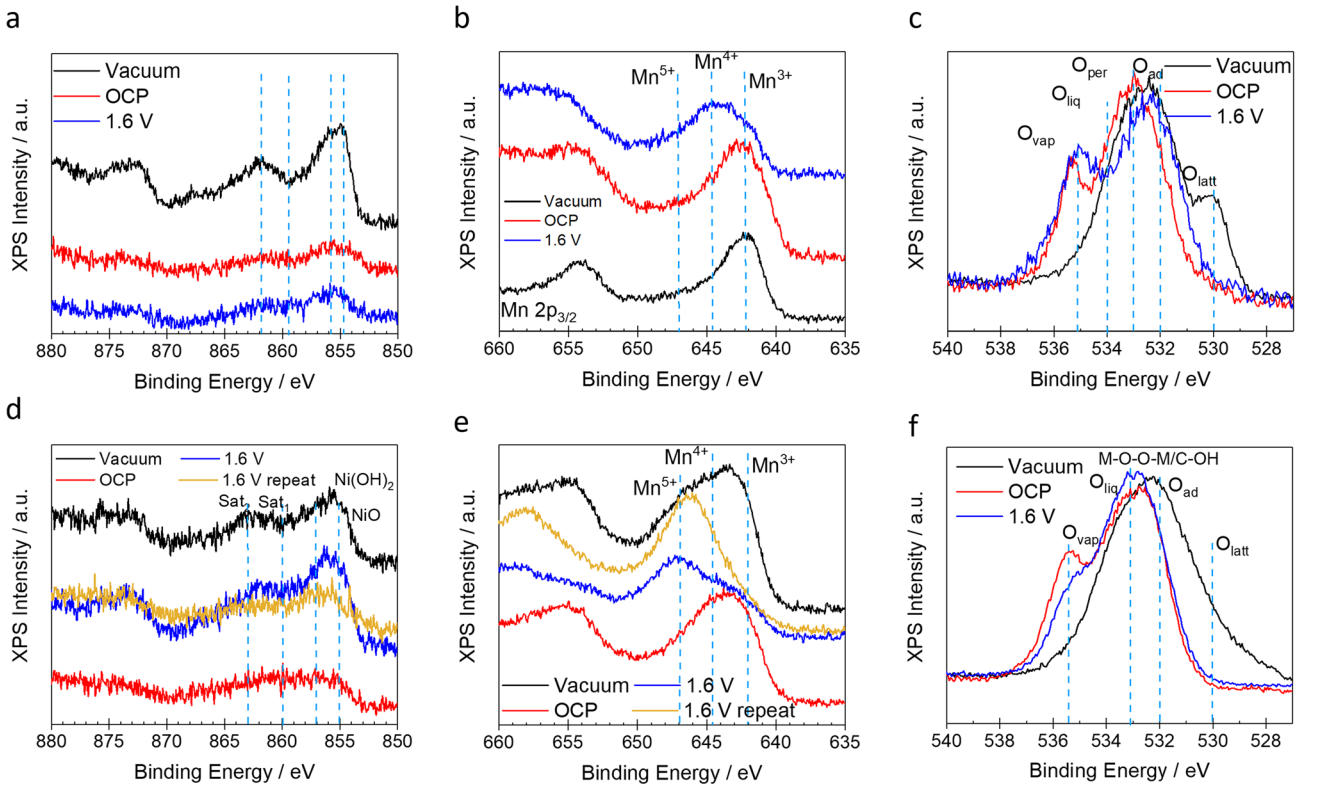

Fig. 6 Operando XPS spectra of $NiMnO_3$ (a) Ni 2p; (b) Mn 2p; (c) O 1s, and $NiMnO_3$–rGO (d) Ni 2p; (e) Mn 2p; (f) O 1s.

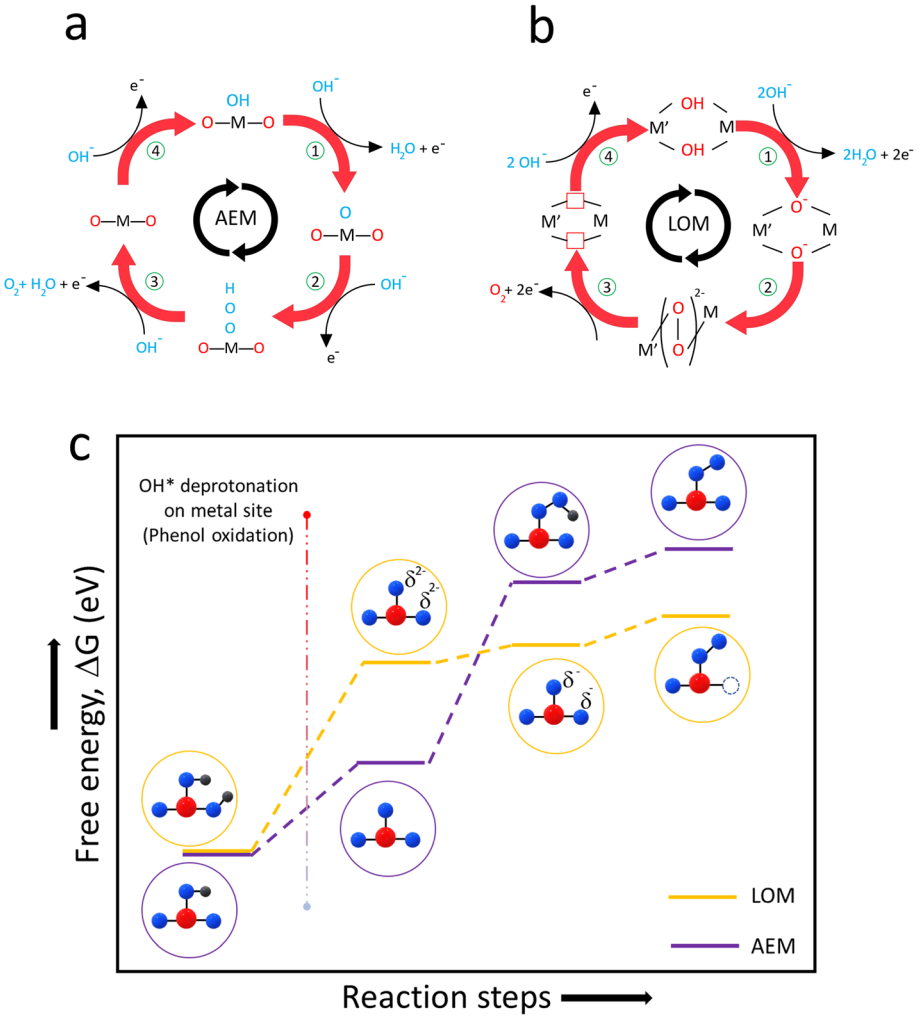

Fig. 7 Proposed OER mechanism over (a) $NiMnO_3$ and (b) $NiMnO_3$–rGO electrocatalysts. (c) Comparison of the OER mechanisms *via* the AEM and LOM.

(Fig. 7c) illustrates the difference: while the AEM pathway relies on metal-centered adsorbates, the LOM pathway involves lattice oxygen redox, leading to a distinct energetic profile that rationalizes the improved kinetics and long-term stability observed for the rGO-containing electrode.

X-ray absorption spectroscopy (XAS), particularly L-edge XAS (or L XAS), is one of the most effective methods for investigating the oxidation states of 3d transition metals using absorption edge positions and spectral characteristics. The NEXAFS spectra are interpreted qualitatively on the basis of line-shape evolution, edge shifts, and relative intensity changes, as full multiplet/crystal-field fitting of transition-metal L-edges is non-trivial and often non-unique; this qualitative analysis, supported by XPS results, is sufficient to track oxidation state and local coordination changes under *operando* conditions. Fig. 8 shows the L-edge XAS spectra of the observed, Ni, Mn L-edge, and O K-edge spectra, during *operando* measurements under real-time OER conditions as a function of applied potentials for pure $NiMnO_3$ (Fig. 8a–c) and $NiMnO_3$–rGO (Fig. 8e and f). The O K-edge spectra in Fig. 8c and f provide complementary information on the involvement of lattice oxygen and the formation of surface hydroxyl terminations (M–OH) and peroxo-like (μ-O) species as the potential increases. The appearance and growth of these species at specific photon energies confirm the progressive oxidation of lattice oxygen and the transformation of adsorbed intermediates, supporting a mechanism where lattice and adsorbed oxygen species interchangeably contribute to O–O bond formation. Very interestingly, as shown in Fig. 8f, at OCP, the intensity of t_{2g} and e_g changes, which is related to the removal of the electrons of oxygen and the increase of holes in the t_{2g} and e_g orbitals, indicating the formation of M–O–O–M bond. Further increase in the applied potential to slightly above OER potential, we observe the oxidation of O moiety as we can see the lowering intensity of t_{2g} orbitals.[36,37] The transition between oxidation states of Ni (Fig. 8a and d) and Mn (Fig. 8b and e), facilitated by their redox flexibility,[38,39] is critical for stabilizing the high-energy intermediates involved in the OER, thereby enhancing the overall catalytic efficiency of the $NiMnO_3$–rGO composite for phenol oxidation.[40]

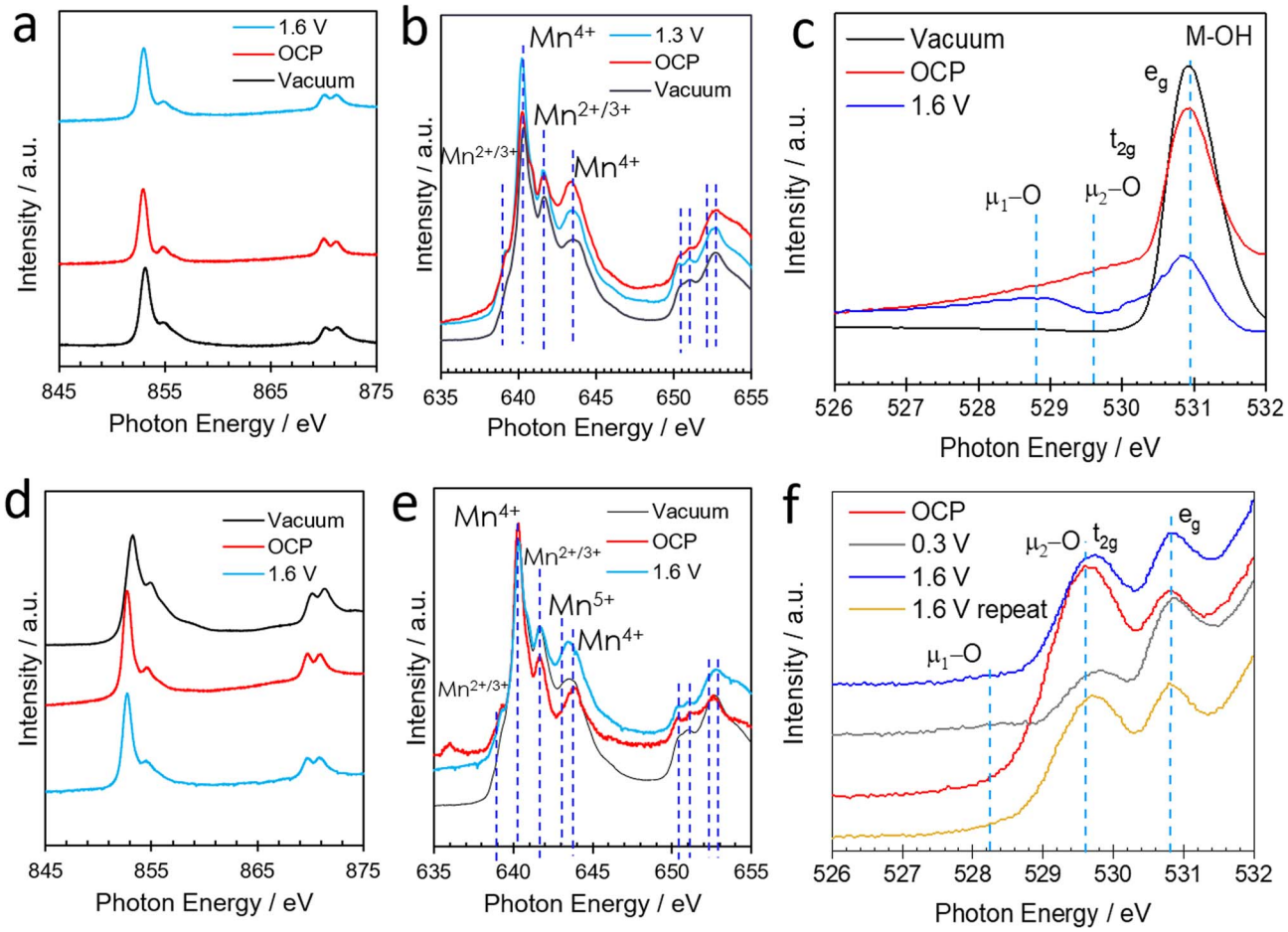

Fig. 8 Operando NEXAFS of $NiMnO_3$ (a) L-edge spectra of Ni; (b) L-edge spectra of Mn; (c) K-edge spectra of O; and $NiMnO_3$–rGO (d) L-edge spectra of Ni; (e) L-edge spectra of Mn; (f) K-edge spectra of O; under real-time OER conditions. Spectra were collected at vacuum, open-circuit potential (OCP), and under applied potentials (1.6 V), illustrating the evolution of both Ni and Mn oxidation states.

Overall, these *operando* XAS observations provide deep insight into the dynamic electronic restructuring of the $NiMnO_3$–rGO catalyst under OER conditions, underscoring the role of LOM. The spectral changes confirm the simultaneous involvement of Ni and Mn centers in stabilizing reactive oxygen species, which promotes sustained $^{\bullet}OH$ generation and is expected to improve the electrocatalyst efficiency and durability in pollutant degradation.

3.5. Stability and post-mortem study

The stability of the $NiMnO_3$–rGO composite on graphite felt (GF/$NiMnO_3$–rGO) and nickel foam (NF/$NiMnO_3$) substrates was assessed by monitoring the cell voltage over 250 h in the electrochemical flow cell under constant current continuous operation. As shown in Fig. 9a, the GF/$NiMnO_3$–rGO electrode maintains a stable value of around 3.25 V throughout the entire test duration, with minimal fluctuation. This voltage stability suggests that the GF-supported composite anode possesses excellent durability and resistance to deactivation under prolonged operation, likely due to the synergistic effects of rGO and the GF substrate. The rGO enhances the electron transfer rate and increases the electrochemical surface area, which may contribute to sustained performance by stabilizing active sites and reducing the risk of catalyst degradation.

In contrast, the NF/$NiMnO_3$ electrode shows a higher initial voltage, followed by fluctuations before reaching a relatively stable value near 3.5 V. The initial instability and the higher starting potential observed with NF/$NiMnO_3$ may be attributed to the less conductive and less stable nature of the NF substrate, which could lead to higher internal resistance and gradual degradation of the electrochemical performance. These fluctuations could also indicate a slower stabilization of the catalyst surface or possible degradation of active sites over time, affecting the electrode efficiency in maintaining a consistent OER rate. The results clearly demonstrate the superior stability of the GF/$NiMnO_3$–rGO material. This finding aligns with the aforementioned enhanced catalytic activity and efficiency of the GF/$NiMnO_3$–rGO electrode in pollutant degradation, further reinforcing its suitability for long-term applications in electrochemical oxidation processes.

To evaluate the structural stability of the GF/$NiMnO_3$–rGO electrode after extended electrochemical testing, SEM images were captured before and after 400 h of continuous operation (the previous test of 250 h was extended for an additional 150 h).

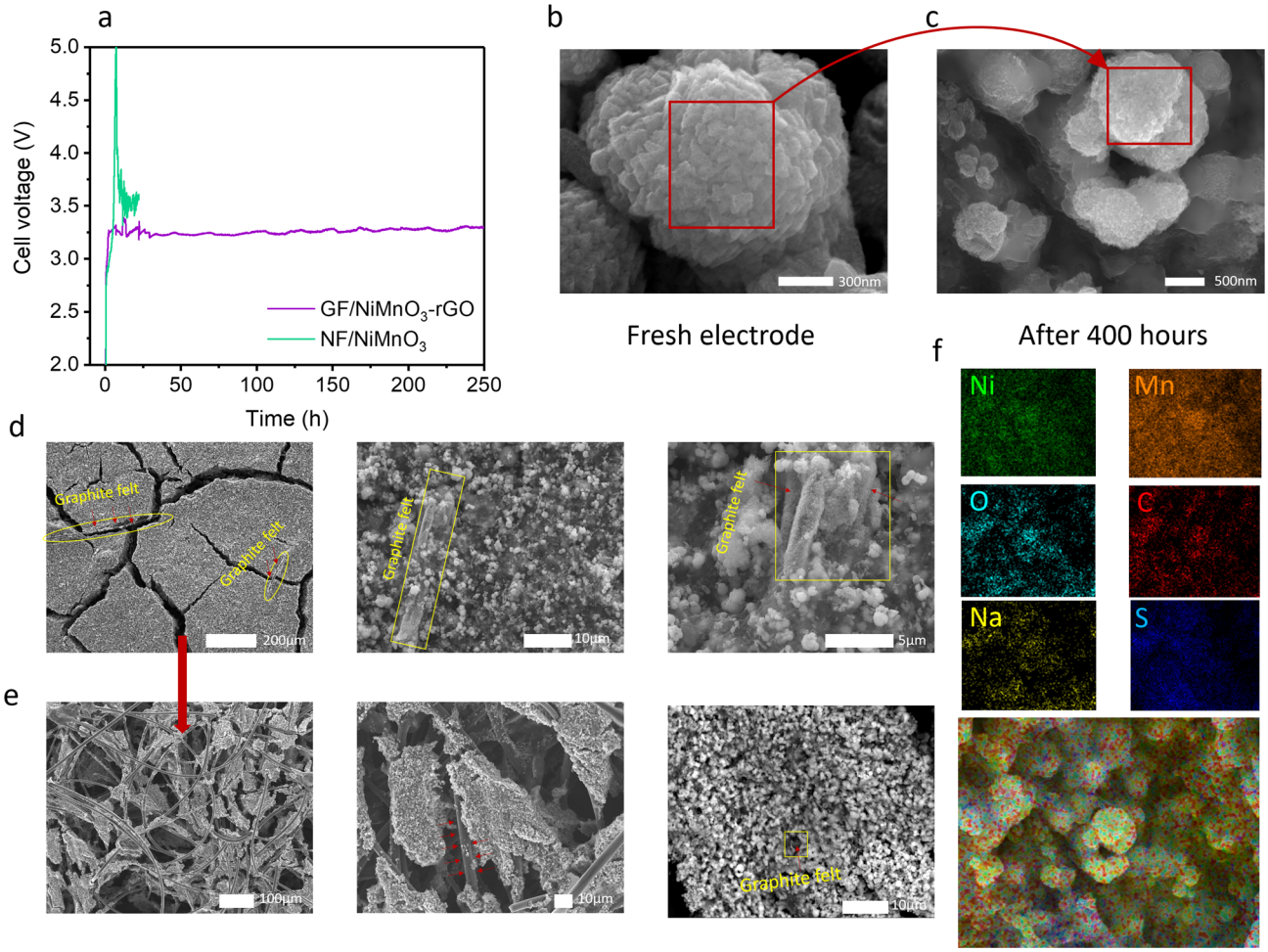

Fig. 9 Stability assessment of GF/$NiMnO_3$–rGO and NF/$NiMnO_3$ electrodes. (a) Electrochemical flow cell experiment under continuous operation for 250 h. (b and c) SEM images of GF/$NiMnO_3$–rGO before and after 400 h of stability testing, respectively, highlighting changes in catalyst particle morphology. (d and e) SEM images of GF/$NiMnO_3$–rGO before and after 400 h of stability testing, respectively, focusing on the distribution of catalyst particles across the GF support. (f) EDS analysis of the anode after 400 h of operation. All experiments were conducted in 0.1 M Na_2SO_4 electrolyte (neutral pH) at a current density of 10 mA cm^{-2}.

The first set of SEM images (Fig. 9b and c) provides higher-magnification views of the particle morphology before and after the stability test. Notably, the individual $NiMnO_3$–rGO particles maintain their original morphology, showing no signs of structural collapse or significant agglomeration after 400 h of operation. The unchanged particle morphology suggests that the $NiMnO_3$–rGO composite itself possesses high structural stability, with the rGO matrix potentially playing a role in preserving particle integrity by mitigating particle agglomeration or collapse under prolonged reaction conditions. In the second set of SEM images (Fig. 9d), taken before testing, the electrode surface exhibits a well-distributed layer of $NiMnO_3$–rGO particles on the GF substrate. These particles are uniformly coated and exhibit a cohesive structure, with no apparent signs of detachment or degradation. This initial morphology indicates a robust integration of the $NiMnO_3$–rGO active material on the substrate. After 400 h of operation, however, the SEM images in Fig. 9e reveal evidence of material loss from the electrode surface. The originally continuous layer of $NiMnO_3$–rGO appears thinner, and certain regions show partial exposure of the underlying GF fibers. This suggests that prolonged electrochemical cycling led to some detachment of the active material, possibly due to gradual wear or mechanical stress under reaction conditions. Despite this material loss, the remaining active layer retains its integrity, covering a substantial portion of the surface, which likely contributed to the electrode sustained performance observed over the test period. These SEM analyses indicate that while there is some material loss on the macro-scale, the microstructure and morphology of the $NiMnO_3$–rGO particles remain stable, which could be attributed to the stabilizing influence of rGO. This partial retention of active material, combined with preserved particle morphology, likely underpins the electrode's overall stability and efficiency, making GF/$NiMnO_3$–rGO a promising candidate for long-term applications despite minor material detachment.

Finally, the EDS analysis performed on the GF/$NiMnO_3$–rGO electrode after 400 h of continuous operation shows that Ni and Mn are uniformly distributed, which suggests that the $NiMnO_3$

active layer remains well-integrated with the rGO and GF substrate, even after prolonged electrochemical cycling (Fig. 9f). This distribution indicates that the $NiMnO_3$–rGO composite structure is stable under extended reaction conditions, as no significant agglomeration or segregation of metal species is observed. The presence of oxygen is consistent with the anticipated formation of oxide layers, which contribute to the OER mechanism through the production of hydroxyl radicals. The uniform oxygen distribution supports the prevalence of the LOM mechanism in OE, as discussed earlier, where lattice oxygen and adsorbed intermediates interact to stabilize O–O bonds and facilitate radical generation.[13,36,41]

Note that, additionally, trace amounts of sodium (Na) and sulfur (S) were detected on the electrode surface, originating from the Na_2SO_4 supporting electrolyte used during the reaction.

4. Conclusions

This study successfully demonstrates the potential of a novel $NiMnO_3$–rGO nanocomposite as an advanced electrode material for electrochemical oxidation in environmental remediation. The integration of rGO enhances electron transfer kinetics and increases the density of electroactive sites, leading to superior electrocatalytic performance. As a result, the GF/$NiMnO_3$–rGO electrode achieved complete (100%) phenol degradation in just 30 min, significantly outperforming the NF/$NiMnO_3$ counterpart. Through *operando* XPS and NEXAFS analysis, it was possible to unveil the underlying OER mechanisms, revealing that $NiMnO_3$–rGO favors $^{\bullet}OH$ production *via* the LOM, whereas $NiMnO_3$ alone primarily follows the AEM. This mechanistic shift, facilitated by the presence of rGO, contributes to greater catalytic efficiency and stability. The GF/$NiMnO_3$–rGO electrode demonstrated exceptional durability, maintaining 100% phenol removal over five consecutive cycles and stable operation for 400 h with minimal material loss. Additionally, its energy consumption remained low at 60–65 Wh per kg COD removed, making it a practical and scalable solution. Overall, these findings highlight $NiMnO_3$–rGO as a promising candidate for electrochemical water treatment, paving the way for future optimizations in electrode design and hybrid systems. Further research should explore its combination with different cathodes to enhance complementary reactions and long-term stability.

Conflicts of interest

The authors declare that they have no known competing financial interests or personal relationships that could have appeared to influence the work reported in this paper.

Data availability

Data will be made available on request.

Supplementary information: procedures used to calculate phenol and COD removal efficiencies, a detailed description of the anode preparation process, and the textural and structural characterization of the active materials. Furthermore, it outlines the rationale for selecting the electrode substrates, as well as a comprehensive description of the electrochemical cell design and the equipment employed during the synchrotron-based XPS and NEXAFS experiments. See DOI: **https://doi.org/10.1039/d5ta05337d**.

Acknowledgements

K. M. acknowledges the HYSOLCHEM project (grant agreement no. 101017928) financed by the EU Horizon 2020 research and innovation program "A Way of Making Europe". I. S. gratefully acknowledges financial support from project PID2022-140378OB-I00, funded by MICIU/AEI/10.13039/501100011033 (Spain) and by ERDF/EU. J. L. recognizes the financial support provided by the project PID2023-153183OA-I00 (NET4BAT, MICIU/AEI/10.13039/501100011033) co-funded by ERDF/EU. J. J. Lado appreciates also the Talento's program of the Community of Madrid (Spain), which involves the project SELECT-VALUE (2020-T1/AMB-19799).

References

1 J. Cai, B. Niu, Q. Xie, N. Lu, S. Huang, G. Zhao and J. Zhao, Accurate removal of toxic organic pollutants from complex water matrices, *Environ. Sci. Technol.*, 2022, **56**(5), 2917–2935, DOI: **10.1021/acs.est.1c07824**.

2 Y. Wen, G. Schoups and N. Van De Giesen, Organic pollution of rivers: Combined threats of urbanization, livestock farming and global climate change, *Sci. Rep.*, 2017, **7**(1), 43289, DOI: **10.1038/srep43289**.

3 N. E. Peters, M. Meybeck and D. V. Chapman, Effects of Human Activities on Water Quality, in *Encyclopedia of Hydrological Sciences*, ed. M. G. Anderson and J. J. McDonnell, John Wiley & Sons, Ltd, Chichester, UK, 2005, p. hsa096, DOI: **10.1002/0470848944.hsa096**.

4 S. Sharma and A. Bhattacharya, Drinking water contamination and treatment techniques, *Appl. Water Sci.*, 2017, **7**(3), 1043–1067, DOI: **10.1007/s13201-016-0455-7**.

5 C. A. Martínez-Huitle, M. A. Rodrigo, I. Sirés and O. Scialdone, A critical review on latest innovations and future challenges of electrochemical technology for the abatement of organics in water, *Appl. Catal. B: Environ.*, 2023, **328**, 122430, DOI: **10.1016/j.apcatb.2023.122430**.

6 W. Li, G. Song, J. Sun and M. Zhou, Electrochemical advanced oxidation processes towards carbon neutral wastewater treatment: A review, *Chem. Eng. J.*, 2024, **480**, 148044, DOI: **10.1016/j.cej.2023.148044**.

7 Q. Yuan, S. Qu, R. Li, Z.-Y. Huo, Y. Gao and Y. Luo, Degradation of antibiotics by electrochemical advanced oxidation processes (EAOPs): Performance, mechanisms, and perspectives, *Sci. Total Environ.*, 2023, **856**, 159092, DOI: **10.1016/j.scitotenv.2022.159092**.

8 M. Panizza and G. Cerisola, Direct And mediated anodic oxidation of organic pollutants, *Chem. Rev.*, 2009, **109**(12), 6541–6569, DOI: **10.1021/cr9001319**.

9 I. Sirés and E. Brillas, Upgrading and expanding the electro-Fenton and related processes, *Curr. Opin. Electrochem.*, 2021, **27**, 100686, DOI: 10.1016/j.coelec.2020.100686.
10 A. Grimaud, O. Diaz-Morales, B. Han, W. T. Hong, Y. -L. Lee, L. Giordano, K. A. Stoerzinger, M. T. M. Koper and Y. Shao-Horn, Activating lattice oxygen redox reactions in metal oxides to catalyse oxygen evolution, *Nat. Chem.*, 2017, **9**(5), 457–465, DOI: 10.1038/nchem.2695.
11 Y. Li, C. J. Miller, L. Wu and T. D. Waite, Hydroxyl radical production via a reaction of electrochemically generated hydrogen peroxide and atomic hydrogen: An effective process for contaminant oxidation?, *Environ. Sci. Technol.*, 2022, **56**(9), 5820–5829, DOI: 10.1021/acs.est.2c00405.
12 Y. Sun, R. R. Chen, C. Biz, A. C. Fisher, M. P. Sherburne, J. W. Ager III, J. Gracia and Z. J. Xu, A discussion on the possible involvement of singlet oxygen in oxygen electrocatalysis, *J. Phys. Energy*, 2021, **3**(3), 031004, DOI: 10.1088/2515-7655/abe039.
13 Z. Wang, W. A. Goddard and H. Xiao, Potential-dependent transition of reaction mechanisms for oxygen evolution on layered double hydroxides, *Nat. Commun.*, 2023, **14**(1), 4228, DOI: 10.1038/s41467-023-40011-8.
14 E. Vidrio, H. Jung and C. Anastasio, Generation of hydroxyl radicals from dissolved transition metals in surrogate lung fluid solutions, *Atmos. Environ.*, 2008, **42**(18), 4369–4379, DOI: 10.1016/j.atmosenv.2008.01.004.
15 P. Guo, L. Xu, T. Yu, P. Zhao, J. Xu and B. Shen, Transition metal in-situ doped BiOBr: Introducing oxygen vacancies to enhance hydroxyl radical generation for improved photocatalytic degradation of toluene, *Sep. Purif. Technol.*, 2025, **354**, 129247, DOI: 10.1016/j.seppur.2024.129247.
16 Y. Nosaka, Molecular mechanisms of oxygen evolution reactions for artificial photosynthesis, *Oxygen*, 2023, **3**(4), 407–451, DOI: 10.3390/oxygen3040027.
17 Y. Yao, C. Huang, Y. Yang, M. Li and B. Ren, Electrochemical removal of thiamethoxam using three-dimensional porous PbO_2-CeO_2 composite electrode: Electrode characterization, operational parameters optimization and degradation pathways, *Chem. Eng. J.*, 2018, **350**, 960–970, DOI: 10.1016/j.cej.2018.06.036.
18 Y. Wang, B. Gu and W. Xu, Electro-catalytic degradation of phenol on several metal-oxide anodes, *J. Hazard. Mater.*, 2009, **162**(2–3), 1159–1164, DOI: 10.1016/j.jhazmat.2008.05.164.
19 J. Zambrano and B. Min, Electrochemical treatment of leachate containing highly concentrated phenol and ammonia using a Pt/Ti anode at different current densities, *Environ. Technol. Innov.*, 2020, **18**, 100632, DOI: 10.1016/j.eti.2020.100632.
20 N. Yang, S. Yu, J. V. Macpherson, Y. Einaga, H. Zhao, G. Zhao, G. M. Swain and X. Jiang, Conductive diamond: synthesis, properties, and electrochemical applications, *Chem. Soc. Rev.*, 2019, **48**(1), 157–204, DOI: 10.1039/C7CS00757D.
21 F. J. Recio, P. Herrasti, I. Sirés, A. N. Kulak, D. V. Bavykin, C. Ponce-de-León and F. C. Walsh, The preparation of PbO_2 coatings on reticulated vitreous carbon for the electro-oxidation of organic pollutants, *Electrochim. Acta*, 2011, **56**(14), 5158–5165, DOI: 10.1016/j.electacta.2011.03.054.
22 J. Ma, C. Trellu, N. Oturan, S. Raffy and M. A. Oturan, Development of Ti/TiO_x foams for removal of organic pollutants from water: Influence of porous structure of Ti substrate, *Appl. Catal. B: Environ.*, 2022, **317**, 121736, DOI: 10.1016/j.apcatb.2022.121736.
23 R. Kötz, H. Neff and S. Stucki, Anodic iridium oxide films, *J. Electrochem. Soc.*, 1984, **131**(1), 72–77, DOI: 10.1149/1.2115548.
24 S. Cherevko, S. Geiger, O. Kasian, N. Kulyk, J.-P. Grote, A. Savan, B. R. Shrestha, S. Merzlikin, B. Breitbach, A. Ludwig and K. J. J. Mayrhofer, Oxygen and hydrogen evolution reactions on Ru, RuO_2, Ir, and IrO_2 thin film electrodes in acidic and alkaline electrolytes: A comparative study on activity and stability, *Catal. Today*, 2016, **262**, 170–180, DOI: 10.1016/j.cattod.2015.08.014.
25 X. Zhang, C. Fu, J. Li, C. Yao, T. Lu and L. Pan, MoO_3/reduced graphene oxide composites as anode material for sodium ion batteries, *Ceram. Int.*, 2017, **43**(4), 3769–3773, DOI: 10.1016/j.ceramint.2016.12.018.
26 K. Mirehbar, J. S. Sánchez, S. Pinilla, F. E. Oropeza, I. Sirés, V. A. de la Peña O'Shea, J. Palma and J. J. Lado, Development of a 3D Ni-Mn binary oxide anode for energy-efficient electro-oxidation of organic pollutants, *J. Environ. Chem. Eng.*, 2024, **12**(3), 112562, DOI: 10.1016/j.jece.2024.112562.
27 P. Kakvand, M. S. Rahmanifar, M. F. El-Kady, A. Pendashteh, M. A. Kiani, M. Hashami, M. Najafi, A. Abbasi, M. F. Mousavi and R. B. Kaner, Synthesis of $NiMnO_3$/C nano-composite electrode materials for electrochemical capacitors, *Nanotechnology*, 2016, **27**(31), 315401, DOI: 10.1088/0957-4484/27/31/315401.
28 X. Fu, F. Bei, X. Wang, S. O'Brien and J. R. Lombardi, Excitation profile of surface-enhanced Raman scattering in graphene–metal nanoparticle based derivatives, *Nanoscale*, 2010, **2**, 1461–1466, DOI: 10.1039/C0NR00135J.
29 D. S. Hall, D. J. Lockwood, C. Bock and B. R. MacDougall, Nickel hydroxides and related materials: a review of their structures, synthesis and properties, *Proceed. Royal Soc. A*, 2015, **471**(2174), 20140792, DOI: 10.1098/rspa.2014.0792.
30 Y.-M. Fan, Y. Liu, X. Liu, Y. Liu and L.-Z. Fan, Hierarchical porous $NiCo_2S_4$-rGO composites for high-performance supercapacitors, *Electrochim. Acta*, 2017, **249**, 1–8, DOI: 10.1016/j.electacta.2017.07.175.
31 J. S. Sanchez, A. Pendashteh, J. Palma, M. Anderson and R. Marcilla, Synthesis and application of $NiMnO_3$-rGO nanocomposites as electrode materials for hybrid energy storage devices, *Appl. Surf. Sci.*, 2018, **460**, 74–83, DOI: 10.1016/j.apsusc.2018.02.165.
32 A. H. Al-khaykanee, S. R. Ghorbani, H. Arabi and R. Ghanbari, $NiMnO_3$-rGO nanocomposites in a cotton-based flexible yarn supercapacitor, *J. Mater. Sci. Mater. Electron.*, 2024, **35**(2), 141, DOI: 10.1007/s10854-023-11868-8.
33 S. Kumar, J. J. C. Counter, D. C. Grinter, M. A. Van Spronsen, P. Ferrer, A. Large, M. W. Orzech, P. J. Wojcik and G. Held, An electrochemical flow cell for operando XPS and NEXAFS

investigation of solid–liquid interfaces, *J. Phys. Energy*, 2024, **6**(3), 036001, DOI: 10.1088/2515-7655/ad54ee.

34 Y. Liu, L. Bai, T. Li, H. Liu, X. Wang, L. Zhang, X. Hao, C. He and S. Guo, MXene-supported NiMn-LDHs as efficient electrocatalysts towards enhanced oxygen evolution reactions, *Mater. Adv.*, 2022, **3**(10), 4359–4368, DOI: 10.1039/D2MA00302C.

35 Z. Wang, N. Hu, L. Wang, H. Zhao and G. Zhao, *In situ* production of hydroxyl radicals via three-electron oxygen reduction: Opportunities for water treatment, *Angew. Chem.*, 2024, **136**(40), e202407628, DOI: 10.1002/anie.202407628.

36 S. Jiang, D. Ren, Y. Lei, H. Suo and W.-H. Lai, Mechanisms of oxygen evolution reaction in metal oxides: Adsorbate evolution mechanism versus lattice oxygen mechanism, *Mater. Lab*, 2023, **2**(2), 220054, DOI: 10.54227/mlab.20220054.

37 X. Liu, Z. He, M. Ajmal, C. Shi, R. Gao, L. Pan, Z. -F. Huang, X. Zhang and J. -J. Zou, Recent advances in the comprehension and regulation of lattice oxygen oxidation mechanism in oxygen evolution reaction, *Trans. Tianjin Univ.*, 2023, **29**(4), 247–253, DOI: 10.1007/s12209-023-00364-z.

38 S. Choi, S. -J. Kim, S. Han, J. Wang, J. Kim, B. Koo, A. A. Ryabin, S. Kunze, H. Hyun, J. Han, S. -C. Haw, K. H. Chae, C. H. Choi, H. Kim and J. Lim, Enhancing oxygen evolution reaction via a surface reconstruction-induced lattice oxygen mechanism, *ACS Catal.*, 2024, **14**(20), 15096–15107, DOI: 10.1021/acscatal.4c03594.

39 A. Davó-Quiñonero, E. Bailón-García, S. López-Rodríguez, J. Juan-Juan, D. Lozano-Castelló, M. García-Melchor, F. C. Herrera, E. Pellegrin, C. Escudero and A. Bueno-López, Insights into the oxygen vacancy filling mechanism in CuO/CeO_2 catalysts: A key step toward high selectivity in preferential CO oxidation, *ACS Catal.*, 2020, **10**(11), 6532–6545, DOI: 10.1021/acscatal.0c00648.

40 A. Erbe, M. F. Tesch, O. Rüdiger, B. Kaiser, S. DeBeer and M. Rabe, *Operando* studies of Mn oxide based electrocatalysts for the oxygen evolution reaction, *Phys. Chem. Chem. Phys.*, 2023, **25**(40), 26958–26971, DOI: 10.1039/D3CP02384B.

41 Q. Ji, B. Tang, X. Zhang, C. Wang, H. Tan, J. Zhao, R. Liu, M. Sun, H. Liu, C. Jiang, J. Zeng, X. Cai and W. Yan, Operando identification of the oxide path mechanism with different dual-active sites for acidic water oxidation, *Nat. Commun.*, 2024, **15**(1), 8089, DOI: 10.1038/s41467-024-52471-7.